Proceedings World Geothermal Congress 2020+1
Reykjavik, Iceland, April - October 2021

Surficial Signatures of Lineaments and Temperatures on Dieng Volcanic Complex (DVC)

Astisiasari, Dyah Rahmawati Hizbaron, Muhammad Anggri Setiawan, Freek van der Meer

Faculty of Geo-Information Science and Earth Observation, University of Twente, Enschede, the Netherlands

a.astisiasari@utwente.nl

Keywords: Dieng Volcanic Complex (DVC), remote sensing, ASTER, Landsat, ALOS PALSAR, lineament, magnetic, land surface temperature, anomaly

ABSTRACT

Dieng Volcanic Complex (DVC), also known as Dieng plateau, is located in the Province of Central Java, Indonesia. The geothermal exploration in this area has been conducted to study its potency, focusing on the subsurface setting through geophysical investigations. This study aimed to integrate the subsurface expression and surficial signature, particularly to observe the spatial correlation between the subsurface structures and surficial lineaments. The magnetic-based structures and ALOS PALSAR-based lineaments were coupled with the ASTER-based surface kinetic temperature (AST_08), as the proxy indicator of thermally active area. Synthesizing the integrated information from the surficial signatures of lineament density and thermal anomalies, with the subsurface reference on magnetic structures, reflected a result ambiguity for its correlation. The clusters of thermal anomalies were coupled with the zones of lower lineament density and higher magnetic anomalies. While conceptually, lower magnetism generally associates with the hydrothermal zone that relates to higher lineament density, promoting structural channels for up-flow transfer. Several reasons to the biased result might be affected by; (a) the widely contrast of input scale, that may carry lower accuracy from down-scaling the remote sensing dataset to meet the scale of magnetic reference; (b) TIR-based temperature may bear topographical-related issue in estimating temperature on steep or rugged terrains; and (c) the complexity in subsurface expressions.

1. INTRODUCTION

The Dieng Volcanic Complex (DVC) is located in the Province of Central Java, Indonesia. It is a broad highland situated at the border of five Districts of Banjarnegara, Wonosobo, Batang, Kendal, and Temanggung. The DVC is hosted in a Quaternary volcanic range, with a total extent of ± 84 km^2 (14 km long and 6 km wide) (van Bergen et al., 2000). The DVC, also known as Dieng plateau, reaches the elevation of up to ± 2.565 meter above the sea level (Zen, 1971) (see Figure 1).

The landscape of the DVC is governed by the rock attributes and its physical processes that can be observed through remote sensing. Remote sensing for geothermal studies has many contributions under the headings of surface manifestations, e.g., gaseous emission, temperature and deformation, mineral mapping, and structural analysis (van der Meer et al., 2014). Remote sensing data may provide subsurface information, and shall be supported by the field dataset to infer the interpretation reliability and reduce fieldwork involved (Gupta, 2018). However, there seem no integrated research that combines the subsurface data with remote sensing-based surficial information (van der Meer et al., 2014).

The geothermal exploratory studies traditionally rely on geophysical prospecting, pertaining to model the reservoir (van der Meer et al., 2014). Geophysical methods have been widely used to observe the geological contrasts on its physical properties (e.g. magnetic susceptibility, seismic velocity, electrical conductivity, and density) (Castro et al., 2018; Dentith & Mudge, 2014; Gadallah & Fisher, 2009). Magnetic method is one of the most common geophysical surveys that is considered relatively simpler, faster, and more cost-effective (Dentith & Mudge, 2014; Gadallah & Fisher, 2009). A magnetic fieldwork covering the DVC area was conducted by the Volcanology Survey Indonesia (VSI) in 1988. It measured the anomalous pattern of magnetic field intensity to study the subsurface geological structure (Simatupang & Setiawan, 1988).

The surficial lineament features presumably reflect the subsurface structures (Leary et al., 1976; Muffler, 1971). In many geothermal fields, fault structures perform as channel-ways of heat fluxes (e.g., hydrothermal fluids, heated gases, up-surging magma) from earth's interior to the ground surface (Gupta, 2018; Qin et al., 2011). Accordingly, lineaments and underground heat source constitute as important proxies for geothermal observation. For example, the relation between structural geology and stratigraphy is essential to observe the functioning of reservoir, cap rocks, and hydrothermal circulation (van der Meer et al., 2014). However, there are several conditions where the subsurface trajectories are not directly linked to the surface expressions, and thus leaving no noticeable surface anomalies (van der Meer et al., 2014), or lacking thermal manifestations, termed as "blind" or hidden system (Cumming, 2016).

This work aimed to explore the surficial lineaments using remote sensing imagery, and to observe its correlation with subsurface structures reference from a former magnetic survey by the VSI in 1988. In account for the correlation, both geological structures were also coupled with the ASTER-based surface temperatures, supporting the indication of thermally active regions. The integration of surficial and subsurface dataset refers to the geothermal conceptual mechanism; which suggests that magnetism-related hydrothermal zone may associate with the structural channels for up-flow transfer, thus possibly emitting thermal radiation on the ground surface.

2. STUDY AREA OF DIENG VOLCANIC COMPLEX (DVC)

The Dieng Volcanic Complex (DVC) is characterized by a prominent caldera or a collapsed structure with volcanic edifices and geothermal manifestations (Harijoko et al., 2010; Nurpratama et al., 2015). Based on its geological aspects, Dieng geothermal field is classified as volcanic-hosted geothermal system (Purnomo & Pichler, 2014), that is associated with the heat transfer of magmatic fluids, pyroclastic, and lava flows, discharged from the conduits and craters (Hochstein & Sudarman, 2015).

The existence of surface thermal manifestations on the DVC area consists of: fumaroles and solfataras, hot springs, mud-pools, phreatic eruptions, near-surface hot water (indicated from craters, maars, and crater-lakes), steaming and altered ground (Allard, et al., 1989; Boedihardi, Suranto, & Sudaman, 1991; Hochstein & Sudarman, 2015; van Bergen et al., 2000; Zen, 1971). Figure 1 displays the distribution of thermal manifestations on the DVC, shown as the red dots.

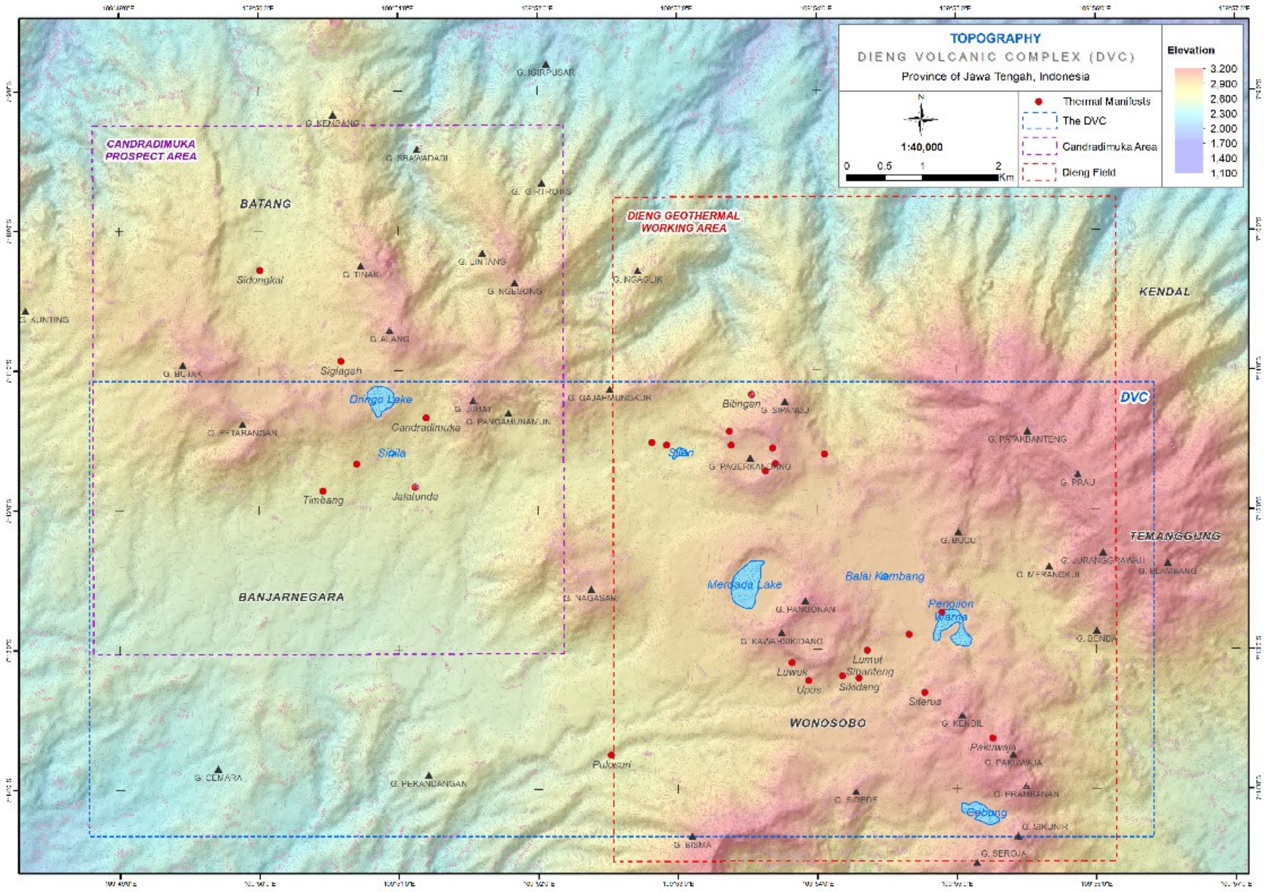

Figure 1: Dieng geothermal area on ALOS PALSAR-based topography. Blue, purple and red rectangles indicate the DVC, Candradimuka prospect area, and Dieng concession area, respectively

Source: (Geo Dipa Energi, 2017b; JAXA/METI, 2010; MEMR, 2017; Pambudi et al., 2015; Sukhyar et al., 1986; Zen, 1971)

3. DATASET

- Geomagnetic reference of Dieng by the VSI, at the scale of 1:100,000 (Simatupang & Setiawan, 1988);
- Shaded relief from ALOS PALSAR RTC, at spatial resolution of 12.5 m (JAXA/METI, 2010);
- ASTER (AST_08); acquisition date: May 5th, 2015 at 03.06.00 UTC, spatial resolution of 90 m (NASA, 2019)
- Rupabumi Indonesia (Indonesia topographic base-map), at the scale of 1:25,000 (BIG, 2006)
- Geologic map of Banjarnegara and Pekalongan Quadrangles, at scale of 1:100,000 (The Geological Agency of Indonesia, 1975);

4. METHODOLOGY

The extraction of remote sensing-based lineament has two identification approaches of: manual delineation and automatic extraction. Manual or visual interpretation depends mostly on the extrapolator subjectivity in delineation process, through surficial reconnaissance (colour, tone, texture, pattern, association). The automatic extraction applies an algorithm to detect the local variance of vector elements from a line of pixels that connected as linear trending on specific direction (Gupta, 2018).

The lineaments reconnaissance depends on the spatial resolution of imageries dataset and its desired output. For example, regional scale of 1:250,000 are able to extract the long and major lineaments for about 5 km in length (e.g. long valleys, tectonic structures, shears, faults, and fractured zones); while large scale of 1:5,000 are able to extract the shorter and minor traces (e.g. faults, fractures, and bedding traces) (Gupta, 2018).

The automatic lineament extraction was commenced by generating shaded reliefs from ALOS PALSAR RTC, with sun illumination coming from eight azimuth directions: 0°, 45°, 90°, 135°, 180°, 225°, 270°, 315°, and 360°. The relief images were combined as a single shaded relief, perpendicular to azimuth illumination. This combined image was processed with LINE module on PCI Geomatica software, with the process of (PCI Geomatics, 2018b, 2018a);

- Edge detection; with Canny algorithm that employs Gaussian filter to produce an edge-strength image. RADI parameter is required as applied filter radius (see Table 1). The resultant is a gradient image of magnitude and direction of edge pixel that is higher than its neighbour pixels. If pixel is not match the threshold, it will have 0 edge strength.
- Threshold setting; gradient image (edge-strength image) setup for a binary-edge image (edge pixel is as an edge or a background). The edge pixels that don't match the gradient threshold are removed. Threshold parameter is GTHR
- Lineament extraction from the binary-edge image. Pixel connectivity or edge linking algorithm was applied to connect pixels identified as linear-edge pixels. Parameters required for this process are: LTHR, FTHR, ATHR, and DTHR

Table 1. Threshold Parameters Setting for Lineament Extraction with LINE Module

Threshold	Paramaters	Unit Range
RADI (Filter Radius)	Radius of Gaussian filter determines the smallest-detail to detect Higher RADI detects lesser detail or noise, thus loss of data	0 – 8192 Pixels
GTHR (Edge Gradient)	Minimum gradient level for an edge pixel. If ON pixels appear too sparse, decrease the value. If too dense & noisy, increase the value	0 – 255 Pixels
LTHR (Curve Length)	Minimum length of curve considered as lineament. Higher value may obtain curvilinear, while lower than threshold is discarded or eliminated	0 – 8192 Pixels
FTHR (Line fitting Error)	Maximum error for fitting polyline segments to a curve. Lower values mean better fitting & shorter segments. Larger values mean longer and straighter segments	0 – 8192 Pixels
ATHR (Angular Difference)	Maximum angle between polyline segments or between 2 vectors to be linked. Angles that exceeds the threshold are segmented into 2 or more vectors	0 – 90 Degrees
DTHR (Linking Distance)	Maximum distance between the end points of two vectors to be linked. Better to detect separately on higher resolution	0 – 8192 Pixels

Source: (Dentith & Mudge, 2014; Harris Geospatial Solutions Inc., 2019b, 2019a; PCI Geomatics, 2018b, 2018a)

Post-processing analysis for the extracted lineaments included the crosscheck and correction with the updated land-cover reference from BIG, 2006. It aimed to remove the unnatural or man-made linear features (e.g., road and drainage networks, agricultural and settlement boundaries), thus retaining only the natural structures.

Statistical analysis for the extracted lineaments can be assessed through its trending direction (the lineament frequency scaled by length), and spatial density (frequency or number per-unit area). The trending direction was assessed through a rose diagram generated from Stereonet software that took the values of: start-end coordinates (angle direction) and lineaments distance.

The density analysis measures the magnitude distribution of lineament concentration per-unit area. The density toolset can perform the analysis with kernel function over the line segments that equals to the line population (ESRI, 2016). Linear features are smoother within the fitted kernel radius, and diminished down to 0 as it distanced away from the radius. The integration between lineament density and magnetic reference by the VSI (Simatupang & Setiawan, 1988) was performed to observe the spatial correlation between surficial lineament signature with the subsurface structural expression.

Land Surface Temperature (LST) on the DVC was estimated based on the ASTER product on Surface Kinetic Temperature (AST_08), that applies TES (Temperature-Emissivity Separation) algorithm on its five Thermal Infrared (TIR) channels (Gillespie et al., 1999; Sobrino et al., 2006). TES algorithm employs surface emissivity values from AST_05 product to scale the emitted radiance and minimize the effect of reflected down-welling irradiance (Abrams & Hook, 2002).

The surficial thermal anomalies were detected from the statistical threshold as differed values from its reference background or neighbouring area (Stober & Bucher, 2013; Wang et al., 2019). The distribution of significant thermal signatures can be spatially patterned by analysing its z-values (standard deviation) and p-values (probability). The Getis-Ord Gi* tool provides spatial analysis to cluster the significant thermal signatures on particular confidence levels (ESRI, 2018). In order to enhance the thermal anomaly clusters associated with thermally active region, the anomaly signatures that were correlated with built-up zones were masked-off with the settlement reference from BIG, 2006.

5. GEOLOGICAL STRUCTURES OF DIENG VOLCANIC COMPLEX

Most of the geothermal fields have the active faulting structures that serve as permeable channels for hydrothermal fluids transfer. This structure can be formed by tension that causes normal faults, or by compression forces that cause reverse or thrust. An active geothermal field usually has normal faults that can break-up the reservoir rocks (Browne, 1984). The channel features along the reservoir rocks can be identified from rock discontinuities, expressed as: faults, fractures, joints, bedding, or fissures (Browne, 1984). These various structures may correspond to linear alignments, occurred as straight, parallel, or curvilinear features (Gupta, 2018). The linear arrangement of geological structures may reflect the subsurface fractures as the weakness zones (Muffler, 1971). Besides, it may also affect the presence of thermal manifestations at the ground surface, as solfatara, fumarole, or hot spring (PVMBG, 2014).

The DVC generally has two separated geothermal system of: Dieng geothermal field on the Eastern sector, and Candradimuka prospect sector on the Western. These sectors fall in continuation on the East–West trending (Muffler, 1971). Figure 2 depicts the redrawn geological structures on the DVC (Boedihardi et al., 1991; Sukhyar et al., 1986), categorized as volcanic and lineament features (Muffler, 1971; Zen, 1971):

- Volcanic center lineaments;

  - The extending E–W from Pagerkandang to Mt. Butak-Petarangan. It extends Westward for ± 50 km from Dieng complex to Mt. Slamet (Miller et al., 1983; Muffler, 1971)
  - The extending NW–SE from Pagerkandang crater to Mt. Pakuwaja. It extends for ± 35 km South-eastward to Mt Sindoro-Sumbing (Miller et al., 1983). Volcanic edifices are thermal belts of Sileri, Sikidang, Pakuwaja (Hino et al., 2013), and Pagerkandang (Muffler, 1971)
- Linear features of faults or fractures;
  - The E–W lineaments, between Batur and Mt. Nagasari, in the Southern part of Candradimuka sector. Lineaments are situated on Rataamba horst, and grabens of Batur and Sidongkal (Muffler, 1971; Sukhyar et al., 1986)
  - NW–SE trending of Kayuabang and Sijeruk faults in the Northern part of Candradimuka sector (Simatupang & Setiawan, 1988; Sukhyar et al., 1986)

Dieng geothermal field on the Eastern part of the DVC has three main structural lineaments that likely control the sector. In order from the oldest to the youngest, these major structural trends are (Boedihardi et al., 1991):

- East–West (ESE–WNW) trending; considered as the oldest lineaments, located on the North part of DVC. This structure aligns the volcanic centers of Mt. Jimat, Mt. Pengamunamun, Mt. Gajamungkur, Mt. Sipandu, Mt. Patakbanteng, and Mt. Prau. This North barrier separates the Sileri sector from Sikidang-Merdada sector
- NW–SE fault orientation; alignment started from Sileri and Sikidang-Merdada (NW sector) to Pakuwaja (SE sector). Thermal manifestation are fumaroles (Sileri-Sikidang) (Hino et al., 2013), altered grounds, and phreatic craters. The SE barrier is called Kendil block and separates Sikidang-Merdada sector from Pakuwaja sector
- N–S (NNE–SSW) direction; considered as the youngest structure that expressed Candradimuka sector (Mt. Butak, Mt. Petarangan, and Dringo) (the NNE sector) and Pakuwaja volcanic lineament (Mt. Kunir, Mt. Prambanan, and Mt. Pakuwaja) on the SSW sector (Newhall & Dzurisin, 1988). Thermal manifestations on this zone are the phreatic craters

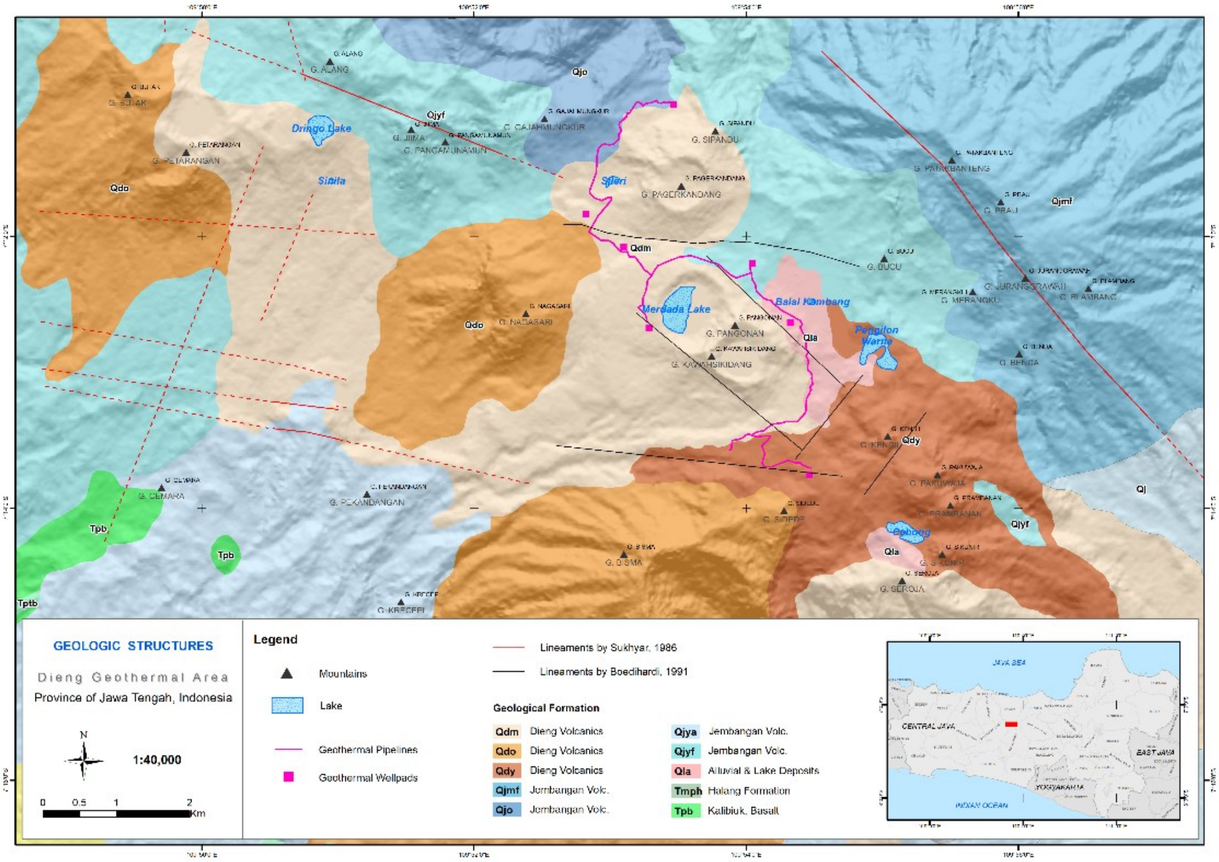

Figure 2: Redrawn lineament structures from Sukhyar et al., 1986 (red lineaments) and Boedihardi et al., 1991 (black lineaments), displayed on the geological map of the DVC

Source: (Boedihardi et al., 1991; Geo Dipa Energi, 2017a; MEMR, 2017; Pambudi et al., 2015; Sukhyar et al., 1986; The Geological Agency of Indonesia, 1975; Zen, 1971)

6. GEOMAGNETIC STUDY ON DIENG VOLCANIC COMPLEX

The Earth has a magnetic field, originated from the electric current flow within the outer core as liquid conductor. The interactions of its convectional and electrical currents can sustain the magnetic field (Gadallah & Fisher, 2009; Jacobs, 1995). The variation of Earth's magnetic field across space and time in terms of intensity and direction (Jacobs, 1998), is related to the existence of Earth's dipoles and geological structures (Dentith & Mudge, 2014; Simatupang & Setiawan, 1988).

Total magnetism is a function given by the sum of both induced and remanent magnetisms. Induced magnetism depends on the magnetic sensitivity of being affected by the Earth's magnetic field; while remanent magnetism is associated with the magnetic mineral content. Magnetic susceptibility reflects the degree of magnetic response, exposed by external magnetic field. It expresses the intensity ratio between induced magnetism and external field that affect it (Dentith & Mudge, 2014).

Magnetic method measures the intensity of Earth's magnetic field, which includes the induced (earth's outer core) and remanent (rocks magnetic mineral) magnetisms (Dentith & Mudge, 2014; Soengkono & Hochstein, 1995). It also characterizes the variation of magnetic susceptibility and contrast of anomalous intensity (Cumming, 2016; Gadallah & Fisher, 2009).

Several main conceptual applications of magnetic surveys for geothermal studies are: (1) magnetite content on sediment-hosted geothermal fields; (2) demagnetization sensitivity on volcano-hosted geothermal fields; (3) magnetic-based structures (faults, stratigraphy); (4) depth to the loss of remnant magnetism (Cumming, 2016); and (5) reservoir characteristics (extent, depth) (Soengkono & Hochstein, 1995).

Almost all of the volcanic host rocks contain magnetic minerals (e.g., magnetite, ilmenite, and titanomagnetite) (Soengkono & Hochstein, 1995). Higher magnetic content exposes higher magnetic values of the basement complex (Gadallah & Fisher, 2009). However, the process of hydrothermal alteration (e.g. carbonation, sulfidisation, and silicification) (Airo, 2002) may partly or completely alter the magnetic primary minerals into non-magnetic minerals (e.g. pyrite, hematite, leucoxene) (Browne, 1984; Dentith & Mudge, 2014; Soengkono & Hochstein, 1995).

The presence of extensive demagnetization or magnetic strength loss in active geothermal fields may reflect the subsurface high permeability and its up-flow pattern (Soengkono & Hochstein, 1995), as the weak region (fault/shear/fracture) of hydrothermal-related zone (Dentith & Mudge, 2014; Soengkono & Hochstein, 1995). Demagnetized rocks are restricted for productive area of high temperature reservoir, as it occurs in extinct geothermal system (Soengkono & Hochstein, 1995).

In 1988, the Volcanology Survey Indonesia (VSI) conducted a magnetic survey in the DVC, to measure the magnetic field intensity and observed its subsurface structure, by measuring 288 points using two magnetometers (Elsec Proton Magnetometer 770 and 595/175). The raw magnetic data from field measurement was processed through: (1) correction for diurnal variation effect; (2) International Geomagnetic Reference Field (IGRF) correction; (3) Upward continuation to attenuate local magnetic anomaly and enhance regional magnetic anomaly; (4) Separation of local anomaly from regional anomaly, by removing the total magnetic anomaly that is already Reduced to Pole (RTP) by regional anomaly (Dentith & Mudge, 2014; Gadallah & Fisher, 2009; Simatupang & Setiawan, 1988). The magnetic anomaly exhibits distinctive deviation of sub-surface response from its surrounding magnetic background. Qualitative interpretation on magnetic anomaly may deduce the geological structures, through the magnetic responses on its direction, magnitude (intensity), and density (Simatupang & Setiawan, 1988).

Figure 5a depicts the redrawn map of total magnetic intensity anomalies and its interpreted structures by Simatupang & Setiawan, 1988. The distribution of higher intensities (positive anomalies) ranged for 395 – 1,485 γ, distributed throughout Sikidang crater, Mt. Saroja, and Mt. Pakuwaja. While the lower intensities (negative anomalies) ranged on -147 – -2,113 γ, covering the areas of Mt. Prau, Mt. Bisma, Sidongkal, and Sijeruk Villages. The wide spreading of low anomalies is possibly associated with magmatic chamber activity, that may devaluate the magnetic intensity (Simatupang & Setiawan, 1988). The interpreted lineaments, suggested fault structures on West–East trending (Batur, Rataamba, and Binangun) and Northwest–Southeast trending on (Mt. Prau and Sijeruk) (Simatupang & Setiawan, 1988).

7. RESULTS

Automatic lineament extraction was commenced by generating the shaded relief as input database, from ALOS PALSAR RTC for eight different illuminating directions: 0°, 45°, 90°, 135°, 180°, 225°, 270°, and 315°. Eight shaded relief images were then combined into a multi-illumination relief (Figure 3).

7.1 Automatic Lineament Extraction

The automatic lineament extraction was processed using LINE module from the PCI Geomatics software. The module parameters thresholds were set as: RADI 10, GTHR 100, LTHR 20, FTHR 1, ATHR 30, and DTHR 30. This threshold combination was constructed through the trial and error process, to consider the optimal result. In comparison to the other settings, this set-up was able to clearly highlight more pronounced features in lesser noise and generalisation.

The extracted lineaments were evaluated and cross-checked, to remove the unnatural structures and retain the natural lineaments, by referring to topographical base-map of Indonesia (BIG, 2006). Figure 4a displays the result of ALOS-based lineaments, extracted from the multi-illumination shaded relief.

The extracted lineaments were statistically analysed through the rose diagram, generated from Stereonet software. Figure 4b represents the graph of petals as lineament frequency scaled by length. Statistically, the maximum direction was in between 91° – 100° (from the North), and the mean direction was on 81.9° (the green arrow). The graph shows three dominant directions on descending order: (a) NE–SW; (b) E–W; and (c) NW-SE trending, that were in conjunction with the magnetic-based directional trends of W–E (Batur-Rataamba) and NW-SE (Mt. Prau and Sijeruk) (Simatupang & Setiawan, 1988).

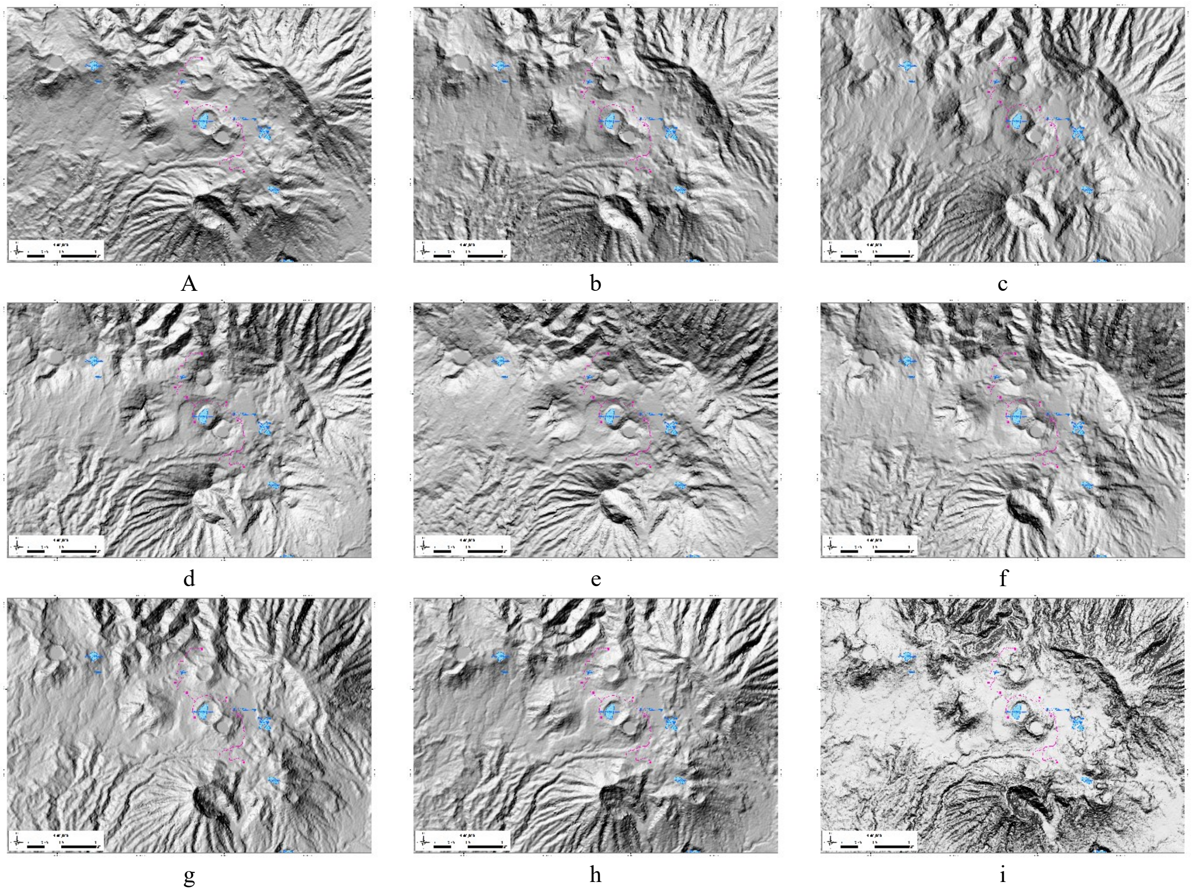

Figure 3: Shaded reliefs of the DVC from 8 azimuth directions of: (a) 0°, (b) 45°, (c) 90°, (d) 135°, (e) 180°, (f) 225°, (g) 270°, (h) 315°, and (i) a combined azimuth direction form 8-illumination angles

Source: (Geo Dipa Energi, 2017b; JAXA/METI, 2010; MEMR, 2017; Pambudi et al., 2015; Sukhyar et al., 1986; Zen, 1971)

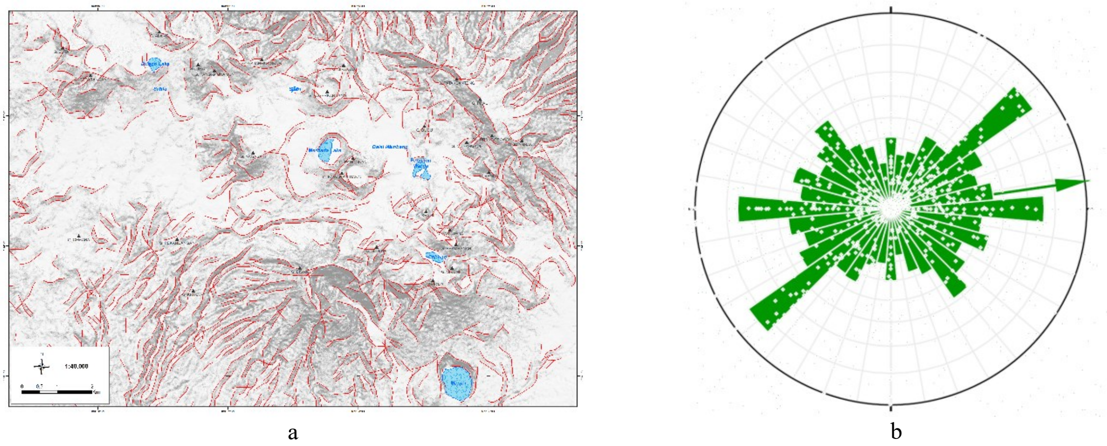

Figure 4: The automatically extracted lineaments based on ALOS PALSAR RTC; (a) Lineament-overlay with ALOS PALSAR-shaded relief; (b) Rose diagram of lineament directions

7.2 Integration of the Extracted Lineaments and Magnetic Reference

The integration of surficial lineaments and subsurface structures was conducted by investigating the correlation between lineaments density and magnetic anomaly. Figure 5 depicts the two dataset to integrate: (a) redrawn magnetic anomaly reference from Simatupang & Setiawan, 1988; and (b) the lineament density (number of lineaments pet-Km^2) with kernel function.

Figure 5b depicts the lineament density using kernel function, ranged from 0 – 7.4 per-Km^2. The spatial distribution of lineament density on the Eastern sector of geothermal field appeared higher than the Western sector of Candradimuka prospect area. Table 2 provides the statistical result of spatial correlation, that showed a significant discrepancy for the correlation between lineament density and magnetic anomaly (as shown from the P-value $< \alpha(.050)$ and low correlation coefficient (r)). The coefficient of determination (R^2) reflected low variance that was accounted as low parameter representation between magnetic anomaly and lineament density.

Referring to Figure 5a, the spatial distribution of total magnetic intensity shows higher anomalies (greenish shades) around the Sikidang crater, Mt. Nagasari, and Mt. Pakuwaja; and lower anomalies around the Mt. Prau, Mt. Bisma, and Batur areas. Visually, the spatial distribution of lineament density appeared to have an inversely similar pattern with the magnetic reference. Higher lineament densities were situated on the relatively steeper terrains (at the rim of Dieng old Caldera, and at volcanic centers of Mt. Butak-Petarangan, Mt. Nagasari, and Mt. Sikidang); while lower densities were majorly spread-out at the center part of the area.

The inverse correlation between lineament density and magnetic anomaly may associate with the magnetic mineral content of volcanic host rocks or hydrothermal alteration process. Higher lineament densities that correspond to lower magnetic anomalies favour the geothermal conceptual mechanism, where lower magnetic response may indicate the hydrothermal alteration zone and its demagnetization aspect. Demagnetization may reflect as the weak zone where more thermal structures have higher chances for hydrothermal alteration occurrence. In account for this, higher surficial lineaments density may indicate higher degree of subsurface fracturing, reflected as lower magnetic zones.

Table 2. Descriptive Statistics for Spatial Correlation between Magnetic Anomaly and Lineament Density

Statistic Elements	
r	-0.234
R^2	0.055
P-value	0.000
Std. Error	479.979

Basic Statistics	Magnetic anomaly (nT)	Lineament density (per-Km^2)
Min	-1963.000	0.000
Max	737.000	5.985
Mean	-370.335	3.008
StdDev	4.156	0.011

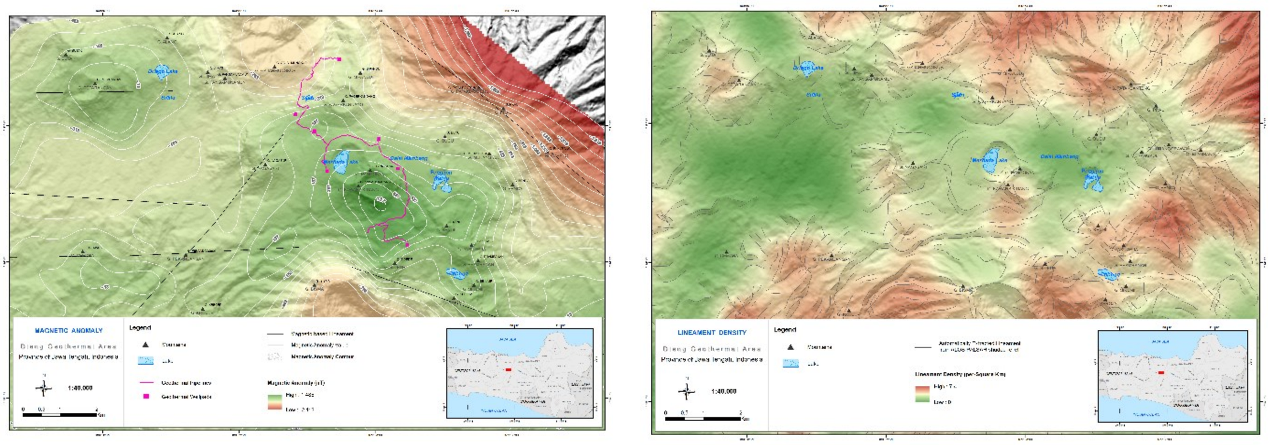

a

b

Figure 5: (a) Redrawn magnetic anomaly from Simatupang & Setiawan, 1988; (b) Lineament density with kernel function

Source: (Geo Dipa Energi, 2017b; JAXA/METI, 2010; MEMR Republic of Indonesia, 2017; Pambudi et al., 2015; Simatupang & Setiawan, 1988; Sukhyar et al., 1986; Zen, 1971)

7.3 Integration of Surface Temperature with Structural Information on Lineament Extraction and Magnetic Reference

Land Surface Temperature (LST) on the DVC area was estimated from the ASTER product on Surface Kinetic Temperature (AST_08). Figure 6a shows the estimated LST ranged for 15.62 – 42.65 °C. The LST has the mean and standard deviation of 25.95 °C and 3.4 °C, respectively. Statistically, the threshold for temperature anomaly was started from 32.77 °C.

Figure 6b shows the cluster distribution of significant thermal anomalies, generated from Getis-Ord Gi* spatial analysis tool, for confidence levels of 95 %. On account to this, the anomaly signatures that were correlated with built-up zones were masked-off with settlements reference from BIG, 2006. Thermal anomalies ranged for 32.85 – 41.95 °C, after the settlements masked-off.

Figure 6c depicts the spatial distribution of thermal anomaly clusters, overlaid on the total magnetic anomalies and lineament density (Figure 6d). The intense thermal anomaly clusters were highlighted at the depression zone of Dieng old caldera. Table 3 summarizes the descriptive statistics of spatial correlation between the thermal anomaly clusters with both of the structural information on lineament densities and total magnetic anomalies.

Statistical analysis was measured on significance level $\alpha(.050)$ for: (a) There were insignificant weak correlations between the thermal anomaly clusters with both of lineament densities and total magnetic anomalies, as shown from the low correlation coefficient (r) and significance P-value > $\alpha(.050)$; (b) Coefficient of determination (R^2) was considered low and reflected data variance that may not represent the parameter population between thermal anomaly clusters with both of the geological structures.

Table 3. Descriptive Statistics for Spatial Correlation between Masked-off Thermal Anomalies with Lineament Density and Total Magnetic Anomaly (TMI)

Elements	Density	Magnetism
Pearson r	0.048	0.078
R^2	0.002	0.006
P-value	0.441	0.209
Std. Error	2.019	2.015

Basic	Density (per-Km^2)	Magnetic anomaly (nT)	Thermal Anomaly Cluster (°C)
Min	0.097	-939.660	32.850
Max	5.504	587.000	41.950
Mean	2.049	-246.601	35.384
StdDev	0.071	14.723	0.125

*Threshold values = Mean + (2 * Std.Dev)

Source: (Dentith & Mudge, 2014; Harris Geospatial Solutions Inc., 2019b, 2019a; PCI Geomatics, 2018b, 2018a)

8. DISCUSSION

Magnetic anomalies with lower values were conceptually associated with demagnetization from the magmatic chamber activity or hydrothermal alteration process. On account of this, the hydrothermally-active regions reflected as weak zones may conform on higher structural density with more chances for alteration process and up-flow transfer. Corresponds to the correlation with thermal anomaly clusters, the lower magnetic anomalies and higher lineament densities were conceptually favoured as thermally active region.

Figure 6c and Figure 6d show the ASTER-based thermal anomaly clusters that were majorly spread throughout the depression zone of the Old Dieng Caldera. Referring to Figure 6c, the distributions of low magnetic zones around Mt. Prau, and Mt. Bisma, expressed low thermal anomalies signatures. In contrary, the spatial distributions of higher magnetism anomalies served more thermal clusters throughout the area. Figure 6d shows thermal anomaly clusters that were more pronounced on the lower-density zones

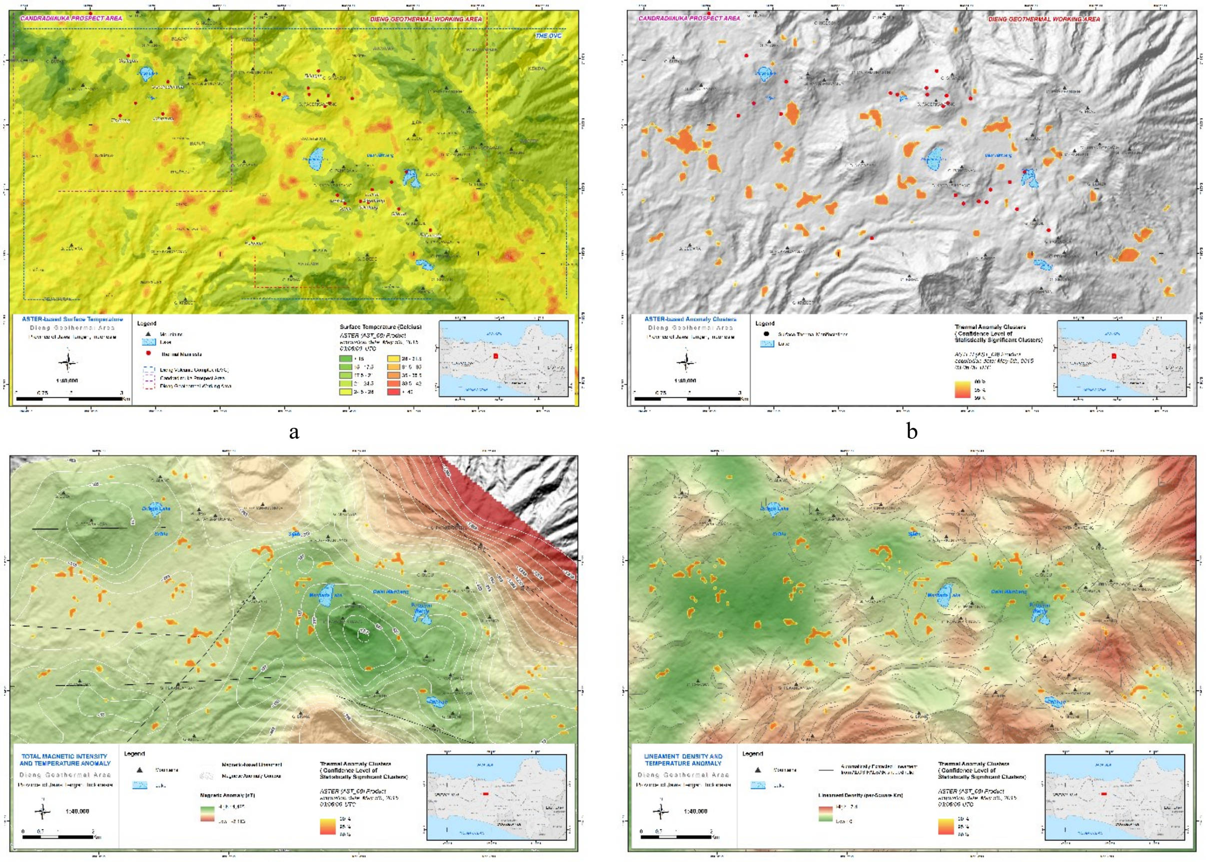

a

b

c

d

Figure 6: Estimated LST from ASTER product on Surface Kinetic Temperature (AST_08); (b) Thermal Anomaly Clusters form Getis-Ord Gi* tool; (c) Masked-off anomaly clusters overlaid on the magnetic reference; (d) Masked-off anomaly clusters overlaid on the lineament density

Source: (Geo Dipa Energi, 2017b; JAXA/METI, 2010; MEMR Republic of Indonesia, 2017; Simatupang & Setiawan, 1988; Sukhyar et al., 1986; Zen, 1971)

To this account, the integration of thermal anomaly clusters with both of the structural information on magnetic anomalies and lineament densities, inferred a spatial correlation ambiguity. The clusters of thermal anomalies were more promoted at lower lineament density and higher magnetic anomalies, than on the zones of higher density and lower magnetism. Several reasons might relate to; (1) widely contrast input scale between the magnetic reference (1:100,000) and ALOS-PALSAR-based lineaments (12.5

spatial resolution) that that may carry lower accuracy from down-scaling the remote sensing dataset to meet the scale of magnetic reference; (2) TIR-based temperature that may bear topographical-related issue for estimation on the steeper terrains; and (3) the complexity in subsurface expressions (e.g. geo-hydrological, physics, and chemistry characteristics)

9. CONCLUSSION

This work integrated the structural information, in order to investigate the correlation between surficial lineaments and subsurface structures. The correlation for both structural dataset was also coupled with the ASTER-based surface temperature, as the proxy indicator of thermally active area.

Analysis on the automatically extracted lineaments based on ALOS PALSAR RTC can be considered through its trending direction (lineament frequency scaled by length) and spatial density (frequency or number per-unit area). The trending directions generated from a rose diagram resulted in: (1) Highest frequency of NE-SW direction in between 91° – 100° (from the North); (2) Three dominant directions (in descending order) of NE–SW, E-W, and NW–SE; (3) Trend directions were in conjunction with the magnetic-based structures that are trending W–E (Batur-Rataamba) and NW-SE (Mt. Prau and Sijeruk) (Simatupang & Setiawan, 1988).

The correlation between the lineament densities with magnetic anomalies resulted in a significant disagreement (P-values $< \alpha(.050)$ and low correlation coefficient (r)). Negative correlation between lineament density and magnetic anomaly supports an inverse relationship that favours the geothermal conceptual mechanism. Higher magmatic anomalies around the volcanic centres may associate with the magnetic mineral content of volcanic host rocks. In contrary, higher lineament densities that correspond to lower magnetic anomalies may indicate demagnetization as a weak region of hydrothermal alteration zone.

In response to the thermal anomaly signatures, the anomaly clusters situated on higher lineament density and lower magnetic zones, were not prevailed. The statistics suggested that there were insignificant weak correlations between the thermal anomaly clusters with both of the structural information on lineament densities and magnetic anomalies, as shown from the low correlation coefficient (r) and significance P-value $> \alpha(.050)$.

Synthesizing the integrated information from the surficial expression on lineament density and thermal anomalies, with subsurface reference on magnetic structures reflected a result ambiguity. Several reasons might relate to; (1) widely contrast input scale between the magnetic reference and ALOS-PALSAR-based lineaments that that may carry lower accuracy from the down-calling remote sensing dataset; (2) ASTER product on surface kinetic temperature (AST-08) might need to be topographically corrected, in order to enhance the thermal signatures on the steeper terrains; and (3) the complexity in subsurface expressions

ACKNOWLEDGMENTS

This work is part of a collaborative Ph.D. research between University of Twente – The Netherlands and University of Gadjah Mada – Indonesia, supported by the GEOCAP (Geothermal Capacity Building Programme) project and LPDP (Indonesian Endowment Fund for Education) scholarship.

REFERENCES

Abrams, M., & Hook, S. (2002). *ASTER User Handbook*.

Airo, M.-L. (2002). Aeromagnetic and aeroradiometric response to hydrothermal alteration. *Surveys in Geophysics*, *23*(October 2001), 273–302.

Allard, P., Dajlevic, D., & Delarue, C. (1989). Origin of carbon dioxide emanation from the 1979 Dieng eruption, Indonesia: Implications for the origin of the 1986 Nyos catastrophe. *Journal of Volcanology and Geothermal Research*, *39*, 195–206.

BIG. (2006). Rupabumi Indonesia. Retrieved from https://portal.ina-sdi.or.id/downloadaoi/

Boedihardi, M., Suranto, & Sudaman, S. (1991). Evaluation of the Dieng Geothermal Field; Review of Development Strategy. In *20th Annual Convention Indonesian Petroleum Association* (pp. 347–361).

Browne, P. R. L. (1984). Lectures on geothermal geology and petrology. Grensasvegur, Reykjavik: UNU Geothermal Training Programme.

Castro, D. L. De, Oliveira, D. C., & Helena, M. (2018). Geostatistical Interplay Between Geophysical and Geochemical Data : Mapping Litho - Structural Assemblages of Mesozoic Igneous Activities in the Parnaíba Basin (NE Brazil). *Surveys in Geophysics*, *39*(4), 683–713. https://doi.org/10.1007/s10712-018-9463-5

Cumming, W. (2016). Geophysics and resource conceptual models in geothermal exploration and development. In R. DiPippo (Ed.), *Geothermal Power Generation Developments and Innovation* (pp. 33–75). Elsevier Ltd. Retrieved from http://dx.doi.org/10.1016/B978-0-08-100337-4.00003-6

Dentith, M., & Mudge, S. T. (2014). *Geophysics for the Mineral Exploration Geoscientist*. New York: Cambridge University Press. Retrieved from www.cambridge.org/9780521809511

ESRI. (2016). Understanding density analysis. Retrieved from http://desktop.arcgis.com/en/arcmap/10.3/tools/spatial-analyst-toolbox/understanding-density-analysis.htm

ESRI. (2018). Hot Spot Analysis (Getis-Ord Gi*). Retrieved from http://desktop.arcgis.com/en/arcmap/10.3/tools/spatial-statistics-toolbox/hot-spot-analysis.htm

Gadallah, M. R., & Fisher, R. (2009). *Exploration Geophysics*. springer-verlag Berlin Heidelberg. https://doi.org/10.1007/978-3-540-85160-8

Geo Dipa Energi. (2017a). Lapangan Existing Geodipa Energy. Retrieved from https://www.geodipa.co.id/bisnis-kami/lapangan-existing/

Geo Dipa Energi. (2017b). Rencana pengembangan Panas Bumi GDE untuk listrik dan non-listrik. Retrieved from https://www.geodipa.co.id/bisnis-kami/pengembangan/

Gillespie, A. R., Rokugawa, S., Hook, S. J., Matsunaga, T., & Kahle, A. B. (1999). Temperature/emissivity separation algorithm theoretical basis document, version 2.4. *Nasa/Gsfc,* ..., 1–64. Retrieved from http://eospso.gsfc.nasa.gov/sites/default/files/atbd/atbd-ast-05-08.pdf

Gupta, R. P. (2018). *Remote Sensing Geology*. *The Photogrammetric Record* (third). springer-verlag, GmbH Germany. Retrieved from https://doi.org/10.1007/978-3-662-55876-8

Harijoko, A., Uruma, R., Wibowo, H. E., Setijadji, L. D., Imai, A., & Watanabe, K. (2010). Long-Term Volcanic Evolution Surrounding Dieng Geothermal Area, Indonesia. In *World Geothermal Congress 2010* (p. 6).

Harris Geospatial Solutions Inc. (2019a). Atmospheric Correction. Retrieved from http://www.harrisgeospatial.com/docs/AtmosphericCorrection.html

Harris Geospatial Solutions Inc. (2019b). Radiometric Calibration. Retrieved from http://www.harrisgeospatial.com/docs/RadiometricCalibration.html

Hino, T., Itoi, R., Tanaka, T., Pambudi, N. A., & Khasani. (2013). Natural state modeling of geothermal reservoir at Dieng, Central Java, Indonesia. *Transactions - Geothermal Resources Council*, *37*(PART 2), 831–835.

Hochstein, M. P., & Sudarman, S. (2015). Indonesian Volcanic Geothermal Systems. *World Geothermal Congress 2015*, (April), 11.

Jacobs, J. A. (1995). The Earth ' s magnetic field and reversals, 166–171.

Jacobs, J. A. (1998). Variations in the intensity of the earth's magnetic field j. a. jacobs. *Surveys in Geophysics*, *19*, 139–187. https://doi.org/https://doi.org/10.1023/A:1006579708430

JAXA/METI. (2010). ALOS PALSAR RTC. https://doi.org/10.5067/Z97HFCNKR6VA

Leary, D. W. O., Friedman, J. D., & Pohn, H. A. (1976). Lineament, linear, lineation: Some proposed new standards for old terms. *GSA Bulletin*, *87*(10), 1463–1469. https://doi.org/10.1130/0016-7606(1976)87<1463

MEMR Republic of Indonesia. (2017). Data of Geothermal Potentials. Retrieved from http://igis.esdm.go.id/igis/potensi/index

Miller, C. D., Sukhyar, R., Santoso, & Hamidi, S. (1983). *Eruptive history of the Dieng mountains region, central Java, and potential hazards from future eruptions*. Denver, CO (USA). Retrieved from https://www.osti.gov/biblio/6940556

Muffler, L. J. P. (1971). *Evaluation of initial investigations Dieng geothermal area, Central Java, Indonesia*.

NASA. (2019). Earthdata Search. Retrieved from https://search.earthdata.nasa.gov/

Newhall, C. G., & Dzurisin, D. (1988). *Historical Unrest at Large Calderas of the World*. *USGS Survey Bulletin* (Vol. 1).

Nurpratama, M. I., Atmaja, R. W., Wibowo, Y. T., Harijoko, A., Husein, S., Sudarno, I., … Utami, P. (2015). Detailed Surface Structural Mapping of the Dieng Geothermal Field in Indonesia. In *World Geothermal Congress 2015* (p. 8).

Pambudi, N. A., Itoi, R., Jalilinasrabady, S., & Jaelani, K. (2015). Performance improvement of a single-flash geothermal power plant in Dieng, Indonesia, upon conversion to a double-flash system using thermodynamic analysis. *Renewable Energy*, *80*, 424–431. https://doi.org/10.1016/j.renene.2015.02.025

PCI Geomatics. (2018a). Edge Detection Filter. Retrieved from http://www.pcigeomatics.com/geomatica-help/references/pciFunction_r/modeler/M_edge.html

PCI Geomatics. (2018b). Lineament Extraction. Retrieved from http://www.pcigeomatics.com/geomatica-help/references/pciFunction_r/python/P_line.html

Purnomo, B. J., & Pichler, T. (2014). Geothermal systems on the island of Java, Indonesia. *Journal of Volcanology and Geothermal Research*, *285*, 47–59. https://doi.org/10.1016/j.jvolgeores.2014.08.004

PVMBG. (2014). G. Dieng, Jawa Tengah. Retrieved from http://www.vsi.esdm.go.id/index.php/gunungapi/data-dasar-gunungapi/531-g-dieng

Qin, Q., Zhang, N., Nan, P., & Chai, L. (2011). Geothermal area detection using Landsat ETM+ thermal infrared data and its mechanistic analysis-A case study in Tengchong, China. *International Journal of Applied Earth Observation and Geoinformation*, *13*(4), 552–559. https://doi.org/10.1016/j.jag.2011.02.005

Simatupang, S. H., & Setiawan, S. (1988). *Pemetaan Geomagnet Komplek G. Dieng Jawa Tengah*. Bandung.

Sobrino, J. A., Jiménez-Muñoz, J. C., Zarco-Tejada, P. J., Sepulcre-Cantó, G., & Miguel, E. de. (2006). Land surface temperature derived from airborne hyperspectral scanner thermal infrared data. *Remote Sensing of Environment*, *102*(1–2), 99–115. https://doi.org/10.1016/j.rse.2006.02.001

Soengkono, S., & Hochstein, M. P. (1995). Application of magnetic method to assess the extent of high temperature geothermal reservoirs. In *Twentieth Workshop on Geothermal Reservoir Engineering* (pp. 71–78). California.

Stober, I., & Bucher, K. (2013). *Geothermal energy - From Theoretical Models to Exploration and Development*. *Fuel and Energy Abstracts* (Vol. 44). springer-verlag Berlin Heidelberg. https://doi.org/10.1007/978-3-642-13352-7

Sukhyar, R., Sumartadipura, N. S., & Effendi, W. (1986). Geologic Map of Dieng Volcano Complex, Central Java. Bandung: Volcaological Survey of Indonesia. Retrieved from http://vsi.esdm.go.id/gallery/picture.php?/70/categories

The Geological Agency of Indonesia. (1975). Geologic Map of the Banjarnegara and Pekalongan Quadrangles, Java. The Geological Agency of Indonesia. Retrieved from https://psg.geologi.esdm.go.id/lexicon/index/384

van Bergen, M. J., Bernard, A., Sumarti, S., Sriwana, T., & Sitorus, K. (2000). Crater Lake of Java : Dieng, Kelud and Ijen. *Excursion Guidebook IAVCEI General Assembly*. Retrieved from https://www.ulb.ac.be/sciences/cvl/DKIPART1.pdf

van der Meer, F., Hecker, C., van Ruitenbeek, F., van Der Werff, H., de Wijkerslooth, C., & Wechsler, C. (2014). Geologic remote sensing for geothermal exploration : A review. *International Journal of Applied Earth Observations and Geoinformation*, *33*, 255–269. https://doi.org/10.1016/j.jag.2014.05.007

Wang, K., Jiang, Q., Yu, D., Yang, Q., Wang, L., & Han, T. (2019). Detecting daytime and nighttime land surface temperature anomalies using thermal infrared remote sensing in Dandong geothermal prospect. *Int J Appl Earth Obs Geoinformation*, *80*(January), 196–205. https://doi.org/10.1016/j.jag.2019.03.016

Zen, M. T. (1971). Geothermal System of the Dieng-Batur Volcanic Complex (pp. 23–38). Bandung.